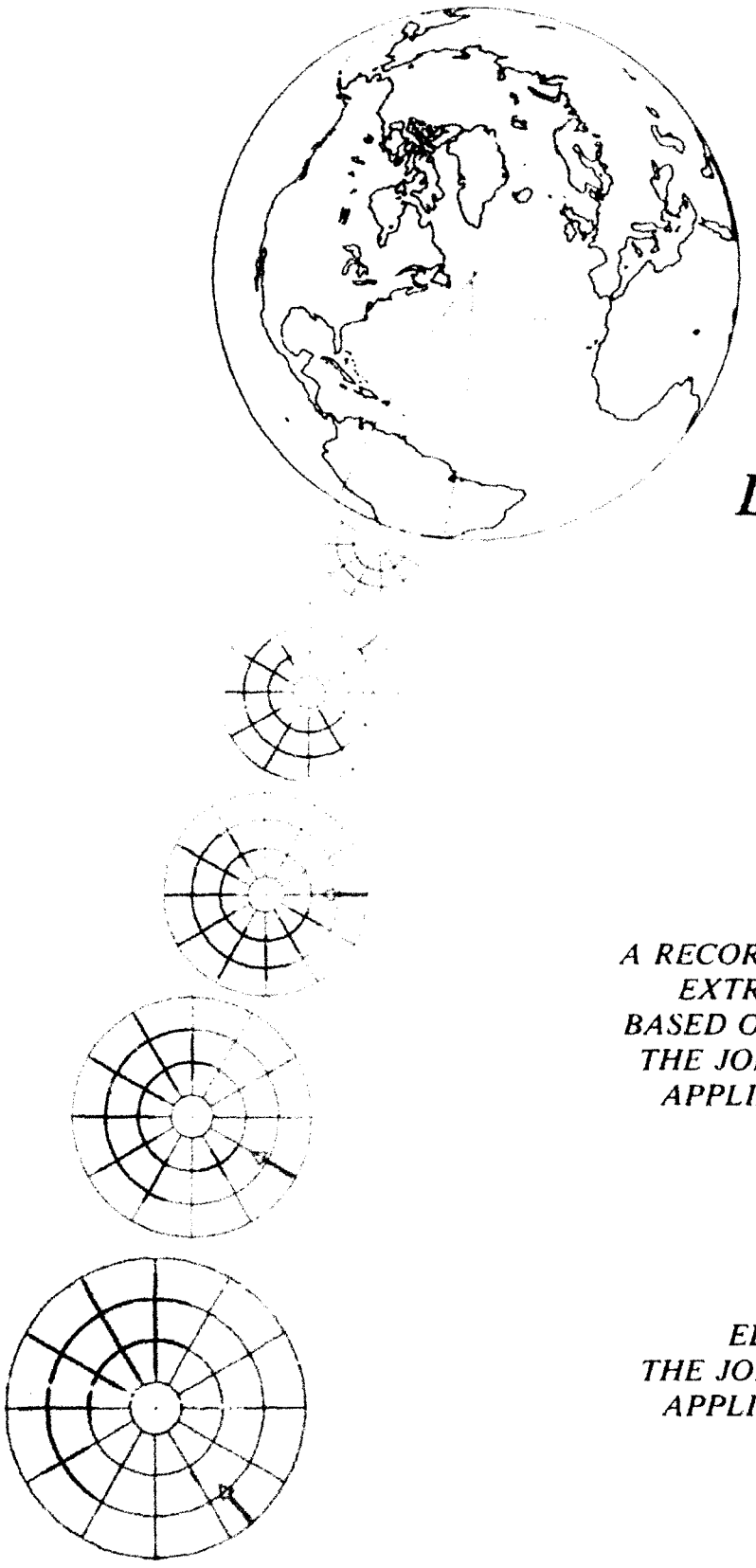

MEASURING
MODELING
PREDICTING
AND APPLYING

DIRECTIONAL OCEAN WAVE SPECTRA

A RECORD OF THE LABRADOR SEA EXTREME WAVES EXPERIMENT BASED ON A SYMPOSIUM HELD AT THE JOHNS HOPKINS UNIVERSITY APPLIED PHYSICS LABORATORY APRIL 18–20, 1989

EDITED BY ROBERT C. BEAL
THE JOHNS HOPKINS UNIVERSITY APPLIED PHYSICS LABORATORY

THE JOHNS HOPKINS UNIVERSITY PRESS
Baltimore and London

Printed in the United States of America

The Johns Hopkins University Press
701 West 40th Street
Baltimore, Maryland 21211-2190
The Johns Hopkins Press Ltd., London

The paper used in this book meets the minimum requirements of American National Standard for Information Sciences—Permanence of Paper for Printed Library Materials, ANSI Z39.48-1984.

Library of Congress Cataloging-in-Publication Data
Directional ocean wave spectra: measuring, modeling, predicting, and applying/edited by Robert C. Beal.
p. cm.—(The Johns Hopkins studies in Earth and space sciences)
"A record of the Labrador Sea Extreme Waves Experiment based on a symposium held at The Johns Hopkins University Applied Physics Laboratory April 18-20, 1989."
Includes bibliographical references and index.
ISBN 0-8018-4261-1 (alk. paper)
1. Ocean waves—Labrador Sea—Congresses. I. Beal, Robert C.
II. Johns Hopkins University. Applied Physics Laboratory.
III. Series.
GC214.L33D57 1991
551.47'02'0916343—dc20 91-16779

KLAUS HASSELMANN, SUSANNE HASSELMANN, CLAUS BRÜNING, and ANNEGRET SPEIDEL

INTERPRETATION AND APPLICATION OF SAR WAVE IMAGE SPECTRA IN WAVE MODELS

A new closed integral transform relation describing the nonlinear mapping of a surface-wave spectrum into a synthetic aperture radar (SAR) image spectrum is presented and applied to selected Labrador Sea Extreme Waves Experiment cases. The new results agree well with observations and with computations using earlier Monte Carlo techniques. The integral transform can be expanded in a series whose terms can be computed rapidly using fast Fourier transforms. The series expansion of the integral transform expression is also useful in identifying the relative contributions of different imaging mechanisms.

INTRODUCTION

Synthetic aperture radars (SAR's) to be flown on ocean satellites and polar orbiting platforms in the 1990s will provide ocean wave modelers for the first time with global measurements of the two-dimensional ocean-wave spectrum. This should bring an unprecedented boost to ocean-wave modeling. But SAR images of the ocean-wave surface are not easily interpreted. They are often strongly nonlinear and show pronounced asymmetries with respect to range and azimuthal imaging. The development of appropriate methods for the efficient processing and assimilation of SAR wave data into ocean-wave models is not straightforward and presents a major challenge to the ocean-wave community.

The basic mechanisms of SAR ocean-wave imaging are nevertheless rather well understood today (cf. Ref. 1). In particular, the characteristic nonlinearity and range-azimuth asymmetry of SAR wave images can be explained by the large azimuthal displacements—compared with the scales of the long waves—of individual backscattering elements in the image plane caused by the orbital motions of the long waves.

To cope with this strong nonlinearity, computations of the transformation of a surface-wave spectrum into a SAR image spectrum have been carried out in the past largely by means of "brute force" Monte Carlo simulations,[2-7] in which a series of random realizations of the sea surface is generated for a given ocean-wave spectrum, and the sea surface is mapped into the SAR image plane, pixel by pixel, for each realization. The SAR images are then Fourier transformed, and the squared Fourier amplitudes are averaged over the ensemble of realizations to obtain an estimate of the image variance spectrum. Typically, 20 to 50 individual sea-surface realizations (40 to 100 degrees of freedom) need to be mapped. The method is relatively costly in computer time and suffers from the usual Monte Carlo statistical sampling uncertainty. Also, it does not offer a simple approach to the inverse problem of estimating the surface-wave spectrum from a measured SAR image spectrum.

Recently, a new closed integral relation for the mapping of a surface-wave spectrum into a SAR image spectrum has been derived by Hasselmann and Hasselmann.[8] Although the transformation is strongly nonlinear, a closed relation between the input surface-wave spectrum and output SAR spectrum could nevertheless be derived by making use of the Gaussian property of the input wave field, which enables all higher order nonlinear dependencies on the input field to be reduced to the surface-wave spectrum.

The closed integral expression can be readily evaluated, after a suitable series expansion, by means of fast Fourier transforms (FFT's). The computing time (less than 1 s per spectrum on a CRAY-2 computer) is short enough for the method to be applied operationally to satellite SAR data. The integral was also evaluated directly without expansion, and although the FFT technique could not be applied, essentially identical results were obtained with comparable computation times for somewhat reduced spectral resolution.

The series expansion of the integral transform relation is also useful in clarifying the role of the various imaging mechanisms. Thus, the relative contributions from hydrodynamic and tilt modulation, from linear velocity bunching, from the interference between these processes, and from higher order nonlinear velocity-bunching interactions can be individually identified as separate spectral terms of the series expansion.

The closed transformation expression has the additional advantage of lending itself readily to inversion by means of iterative inverse modeling methods. Details are given in Ref. 8.

In this article, the results of the theory are summarized and applied to examples from the Labrador Sea Extreme Waves Experiment (LEWEX), using as input hindcast wave spectra computed with the WAM wave model.[9] The theory is verified by comparing the new computations with the Monte Carlo simulations.

CONCEPTS AND NOTATIONS

To discuss meaningfully the new transformation relation presented in the next section and interpret its subsequent application to LEWEX SAR spectra, some basic

concepts and notation need to be introduced. See Ref. 1 for a review of the standard two-scale theory of SAR imaging of a surface-wave field on which these concepts are based. The derivation of the spectral transformation relation is given in Ref. 8.

It is convenient to regard the SAR surface-wave image as the result of two consecutive imaging mechanisms: the cross-section modulation that produces the frozen surface image, $I^R(r)$, and the additional motion effects that, together with the frozen surface contribution, yield the net SAR image, $I^S(r)$, where r is the position vector.

The Frozen Surface Contribution

The frozen surface image, $I^R(r)$, of a linear ocean-wave field corresponds to the image that would be obtained by a real aperture radar (RAR). To a good approximation, it can be linearly related to the surface-wave field.

The surface-wave elevation $\zeta(r, t)$ of a linear ocean-wave field can be decomposed into a superposition of freely propagating wave components:

$$\zeta(r, t) = \int dk \, \{\zeta(k) \exp(i[k \cdot r - \omega t]) + \text{complex conjugate}\} , \quad (1)$$

where $\omega = \sqrt{gk}$ is the gravity-wave frequency, t is time, ζ is the wave height, i designates the "imaginary part of," and k is the wave number vector. To avoid a proliferation of symbols, we shall use the some symbol for a function and its Fourier transform, distinguishing the two where necessary by their arguments. If the RAR imaging mechanism is linear, the variations of the (specific) backscattering cross section, $\sigma(r, t)$, can be similarly decomposed into free wave components:

$$\sigma(r, t) = \bar{\sigma}\{1 + \int dk \, [m(k) \exp(i[k \cdot r - \omega t]) + \text{complex conjugate}]\} , \quad (2)$$

where the cross-section modulation, $m(k)$, is linearly related to $\zeta(k)$ through a modulation transfer function (MTF), $T^R(k)$,

$$m(k) = T^R(k) \, \zeta(k) , \quad (3)$$

and $\bar{\sigma}$ denotes the space-time averaged cross section.

The RAR MTF, $T^R(k)$, can be further decomposed into tilt and hydrodynamic contributions:

$$T^R(k) = T^t(k) + T^h(k) . \quad (4)$$

The tilt and hydrodynamic MTF's have been discussed in detail by various authors.[5, 10-13] For the general theory, however, we require only the net frozen surface MTF, $T^R(k)$, without invoking its decomposition into tilt and hydrodynamic components. We point out also that although we present here a quantitative closed theory for the imaging mechanism as such, the details of the hydrodynamic MTF required as input (and its possible nonlinear corrections) are still only poorly known and need further study.

The frozen surface SAR image represents a snapshot of the field $\sigma(r, t)$ at a particular time, say $t = 0$. Measuring the image modulation intensity $I^R(r)$ (after subtraction of the mean) in units of the normalized cross section, $\sigma(r, 0)/\bar{\sigma}$,

$$I^R(r) = \frac{\sigma(r, 0)}{\bar{\sigma}} - 1 , \quad (5)$$

and introducing the Fourier integral,

$$I^R(r) = \int dk \, I^R(k) e^{ik \cdot r} , \quad (6)$$

we have, from Equation 2,

$$I^R(k) = m(k) + m(-k)^* , \quad (7)$$

where the asterisk indicates a complex conjugate. We have ignored here the SAR system MTF. It appears simply as an additional factor in Equation 7 that we may regard as absorbed in the definition of $m(k)$.

We have also ignored, for simplicity, distortion effects because a side-looking radar does not, in fact, make a field snapshot image but builds up the image from a sequence of consecutively imaged snapshot strips. Thus, moving waves are imaged with slightly Doppler displaced "wave numbers of encounter." (This straightforward geometric effect applies equally for a RAR and a SAR and should be distinguished from the SAR motion effects summarized in the following section.)

Finally, we have not considered clutter effects. To first order, they may simply be represented as an additional clutter noise spectrum superimposed on the image spectrum discussed here.[14]

We note that according to Equation 7,

$$I^R(k) = I^{R*}(-k) , \quad (8)$$

in accordance with the reality condition for a frozen two-dimensional surface, whereas $\zeta(k)$, $\zeta(-k)$ and, similarly, $m(k)$, $m(-k)$ refer to different time-dependent wave components propagating in opposite directions and which, therefore, are not related.

In terms of the directional wave spectrum $F(k)$, defined by

$$\langle \zeta^*(k) \zeta(k') \rangle = \delta(k - k') \frac{F(k)}{2} \quad (9)$$

(where the angle brackets denote ensemble means) such that

$$\langle \zeta^2 \rangle = \int F(k) \, dk , \quad (10)$$

and the frozen surface SAR image variance spectrum $P^R(k)$ is defined by

$$\langle I^{R*}(k) I^R(k') \rangle = \delta(k - k') P^R(k) , \quad (11)$$

with

$$\langle I^{R^2} \rangle = \int P^R(k)\, dk \ , \tag{12}$$

the linear amplitude relations (Eqs. 3 and 7) translate into the linear relation

$$P^R(k) = \tfrac{1}{2}\,[|T^R(k)|^2\, F(k) + |T^R(-k)|^2\, F(-k)] \ . \tag{13}$$

Motion Effects

We limit the discussion of motion effects to pure velocity bunching. Higher order acceleration smearing can be included in the general theory,[8] but it is usually small and will be ignored here for simplicity.

Velocity bunching arises through the variable azimuthal displacements, ξ, of individual backscattering elements in the image plane caused by the spatially variable long-wave orbital velocities. According to standard SAR theory,

$$\xi = \beta v \ , \tag{14}$$

where v is the range component of the local long-wave orbital velocity advecting the small-scale backscattering element, and

$$\beta = \rho/U \ , \tag{15}$$

where ρ is the slant range and U is the platform velocity.

For displacements that are small compared with the characteristic wavelength of the long waves, the velocity-bunching mechanism can be linearized and described by a velocity bunching MTF:

$$T^{vb}(k) = -i\beta k_x T^v(k) \ , \tag{16}$$

where the orbital velocity MTF is

$$T^v(k) = -\omega\left(\sin\theta \frac{k_l}{|k|} + i\cos\theta\right) \ , \tag{17}$$

The SAR image spectrum is then given by the linear expression

$$P^S(k) = \tfrac{1}{2}[|T^S(k)|^2 F(k) + |T^S(-k)|^2 F(-k)] \ , \tag{18}$$

where the net SAR MTF is

$$T^S(k) = T^R(k) + T^{vb}(k) \ . \tag{19}$$

The index S refers here and in the following to the SAR image, including motion effects, while the index R refers, as before, to the frozen surface RAR image.

The linear theory has only limited applicability. As will be shown later, it breaks down in all cases, even for low sea states, for high azimuthal wave numbers. The general nonlinear transformation expression presented in the next section yields, to lowest order, a simple quasi-linear generalization of Equation 18 containing an additional nonlinear azimuthal cutoff factor. This is found to be quite widely applicable and provides a reasonable qualitative description of the SAR spectrum, even in strongly nonlinear cases.

The above relations define all quantities needed to write the general spectral nonlinear transfer expression, with the exception of three autocovariance and covariance functions, which are formed from quadratic products of the fields v and I^R at time lag zero and finite spatial lag r:

$$f^v(r) = \langle v(x + r)v(x)\rangle = \int F(k)|T^v(k)|^2 \exp(ik \cdot r)\, dk \ , \tag{20}$$

$$f^R(r) = \langle I^R(x + r)I^R(x)\rangle = \int \tfrac{1}{2}(F(k)|T^R(k)|^2 + F(-k)|T^R(-k)|^2)\exp(ik \cdot r)\, dk \ , \tag{21}$$

$$f^{Rv}(r) = \langle I^R(x + r)v(x)\rangle = \int \tfrac{1}{2}(F(k)T^R(k)T^v(k)^* + F(-k)T^R(-k)^*T^v(-k)\ \exp(ik \cdot r)\, dk \ . \tag{22}$$

THE CLOSED NONLINEAR SPECTRAL TRANSFORMATION RELATION

The general nonlinear spectral transformation relation derived in Ref. 8 is presented in two forms: as a closed nonlinear integral transform expression, and as a power series expansion. The general integral form does not lend itself readily to computation by fast transform techniques, whereas the terms of the power series expansion can be evaluated individually by fast Fourier transforms. Thus, the expansion form can usually be computed more rapidly. The decomposition into a series also provides a clearer picture of the interplay of the various linear and nonlinear imaging mechanisms in the formation of the final image.

The transform was computed both by direct integration (using a lower resolution representation of the spectrum) and by the fast Fourier transform expansion method. The results were essentially identical.

The closed integral expression has the form

$$P^S(k) = (2\pi)^{-2}\exp[-k_y^2\xi'^2]\int dr\, e^{-ik\cdot r}\exp[k_y^2\beta^2 f^v(r)] \times \{1 + f^R(r) + ik_x\beta[f^{Rv}(r) - f^{Rv}(-r)] + (k_x\beta)^2[f^{Rv}(r) - f^{Rv}(0)]\,[f^{Rv}(-r) - f^{Rv}(0)]\} \ , \tag{23}$$

where

$$\xi' = \beta\,\langle v^2\rangle^{1/2} \tag{24}$$

is the root mean square azimuthal displacement.

The power series expansion is obtained by expanding the second exponential factor in Equation 23. (It is the dependence of this factor on k_y^2 that destroys the otherwise straightforward Fourier transform structure of the integral.) One obtains a series of the form

$$P^S(\boldsymbol{k}) = \exp(-k_x^2\xi'^2) \sum_{n=1}^{\infty} \sum_{m=2n-2}^{2n} (k_x\beta)^m P^S_{nm}(\boldsymbol{k}) , \tag{25}$$

where the index n indicates the order in nonlinearity with respect to the input wave spectrum, and the index m the order with respect to the velocity-bunching parameter β (which is seen to occur always in combination with the azimuthal wave number k_x).

Explicitly,

$$P^S_{n,2n} = \frac{1}{n!}\Omega_n\{f^V(r)^n\} \tag{26}$$

$$P^S_{n,2n-1} = \Omega_n\left\{\frac{i[f^{RV}(r) - f^{RV}(-r)]f^V(r)^{n-1}}{(n-1)!}\right\} \tag{27}$$

$$P^S_{n,2n-2} = \Omega_n\left\{\frac{1}{(n-1)!} f^R(r)f^V(r)^{n-1} + \frac{1}{(n-2)!}[f^{RV}(r) - f^{RV}(0)] \times [f^{RV}(-r) - f^{RV}(0)]f^V(r)^{n-2}\right\} , \tag{28}$$

where Ω_n denotes the Fourier transform operator

$$\Omega_n = (2\pi)^{-2}\int d\boldsymbol{r} \exp(-i\boldsymbol{k}\cdot\boldsymbol{r}) \tag{29}$$

and n runs through all positive integers 1, 2, ... For nonpositive integers, the factorial function is defined as $0! = 1$ and $[(-1)!]^{-1} = 0$. We have left out a term $P_{0,0}$ in the sum representing an irrelevant δ-function contribution at $\boldsymbol{k} = 0$ arising from the mean image intensity.

Summation over the velocity-bunching index m for fixed nonlinearity order n yields a stratification of the expansion with respect to the nonlinearity only:

$$P^S(\boldsymbol{k}) = \exp(-k_x^2\xi'^2) \times \left(P_1^S(\boldsymbol{k}) + P_2^S(\boldsymbol{k}) + \ldots P_n^S(\boldsymbol{k}) + \ldots\right) . \tag{30}$$

The linear term, P_1^S, is found to be identical (as it must be) to the linear SAR spectrum of Equation 18.

The computation of $P^S(\boldsymbol{k})$ according to Equations 25 or 30 involves three steps:

1. Computation of the three autovariance and covariance functions $f^V(r)$, $f^R(r)$, and $f^{RV}(r)$ using the Fourier transform relations 20, 21, and 22.
2. Computation of the various covariance product expressions in Equations 26 through 28.
3. Computation of the Fourier transforms of the covariance product expressions, yielding the series 25. (If there is no need to stratify the expansion with respect to nonlinearity order, the covariance products of different nonlinearity order n for given velocity-bunching order m can be collected together and Fourier transformed in a single operation.)

Since only Fourier transforms are involved, the computations are relatively fast. The complete transformation can be computed in less than 1 s on a CRAY-2. (The computations could also be carried out efficiently on a personal computer with hard-wired fast Fourier transform.) Good convergence is normally achieved even for strongly nonlinear spectra for $n \approx 4$ to 6. The contributions from the higher order terms are concentrated mainly in the neighborhood of the (normally not very important) azimuthal cutoff regions.

As a check, the integral (Eq. 23) was also evaluated directly. The wave-number coordinates were transformed to frequency-direction coordinates, and the integral was computed using the relatively low resolution of the wave model (30° directional resolution and a logarithmic frequency discretization with $\Delta\omega/\omega = 0.1$). The computation time was comparable with the fast Fourier transform expansion method, and the results were virtually identical.

An important feature of the expansions 25 and 30 is the occurrence of the common (nonlinear) azimuthal cutoff factor

$$C = \exp(-k_x^2\xi'^2) . \tag{31}$$

Without inclusion of this azimuthal cutoff factor, the straightforward linear approximation $F_1^S(\boldsymbol{k})$ must always break down at high azimuthal wave numbers, even for low sea states, since real wave spectra, and therefore also F_1^S, decay as a power of the wave number at high wave numbers, rather than exponentially, as required by Equation 30.

In contrast, the lowest order quasi-linear approximation

$$P^S(\boldsymbol{k}) = \exp(-k_x^2\xi'^2)P_1^S(\boldsymbol{k}) \tag{32}$$

of Equation 30, with inclusion of the nonlinear azimuthal cutoff factor, remains a valid approximation for the entire spectrum. In practice, Equation 32 was found to yield a reasonable quantitative approximation for about half the SEASAT and LEWEX SAR spectra studied in Ref. 15 and by C. Brüning and L. F. Zambresky (personal communication), and was successful in capturing the qualitative features of the SAR spectrum in all cases.

If applied as a first approximation in the inverse mapping problem, the quasi-linear form can be immediately inverted analytically (for given ξ'). The solution can then be used to construct a general iterative inversion method for estimating wave spectra from observed SAR spectra.[8] The method gave good convergence in both linear and strongly nonlinear cases.

The existence of a common azimuthal cutoff factor (Eq. 31) acting on all terms of the spectral expansion (Eq. 30) has a useful practical application. Since the cutoff scale ξ' can be readily determined for any SAR spectrum, regardless of the details of the nonlinear imaging process, it provides a robust estimate of a useful integral wave parameter: the root mean square orbital velocity component in the range direction.

It is of interest that Beal et al.,[16] Lyzenga,[5] and Monaldo and Lyzenga[17,18] have already noted empiri-

cally that the observed azimuthal cutoff scale appeared to be proportional to the total root mean square orbital velocity integrated over the entire long-wave spectrum (or some similar integral wave parameter). Previously, this finding had been difficult to interpret theoretically. The frequently used SAR two-scale model, in which an additional scale separation is introduced at the SAR resolution scale, yields an explicit azimuthal smearing given by the so-called "velocity spread" term (cf. Refs. 1 and 19). This is determined by the subresolution scale contribution to the root mean square orbital velocity, i.e., by the integral over only the high wave-number tail of the long-wave orbital velocity spectrum. Tucker[19] computed the effect of this smearing and obtained a filter function that was identical to our form C (Eq. 31), but with ξ' replaced by the root mean square azimuthal displacement (the velocity spread) arising from only the short subresolution scale waves. The present closed transformation theory indicates that the nonlinear velocity bunching from the longer waves must also contribute to the azimuthal smearing, and that the net effect of both short and long waves can be expressed very simply by the azimuthal cutoff factor C—in accordance with Beal et al.[16] and Lyzenga's[5] findings.

APPLICATION TO LEWEX

As an illustration, we apply the transform relation to two LEWEX cases. The input wave spectra for the transformation computations were taken from the observed directional wave buoy (Wavescan) data and from a wave hindcast using the WAM third-generation wave model.[9] Comparison of the hindcast wave fields with wave-buoy observations indicated that the hindcast was acceptable as a first guess, although some systematic deviations were found (cf. Fig. 1). The cases were selected from larger data sets that were analyzed as part of a more extensive wave hindcast study (C. Brüning and L. F. Zambresky, personal communication).

The principal SAR parameters of the two runs are listed in Table 1. The polarization was horizontal-horizontal and the look direction to the right for both runs. The damping factor and wind input modulation term in the hydrodynamic MTF were set equal to zero. The images for both runs were taken over essentially the same wave field, but the two SAR flight directions were opposite, and the aircraft altitude and thus the β parameters (ρ/U) differed by a factor of nearly two.

Figures 1 and 2 compare the observed and computed SAR spectra for the two runs. The two rows in the

Table 1. SAR parameters for two LEWEX runs on 14 March 1987 at the *Tydeman* (50°N latitude, 45°W longitude); the flight speed was 128 m/s and the incidence angle was 52°.

Run	Time (UT)	Flight direction (deg)	Altitude (m)	Slant range, ρ (m)	Range-to-velocity ratio, β
1	1219	89	3688	5990	46.8
2	1259	270	6096	9902	77.4

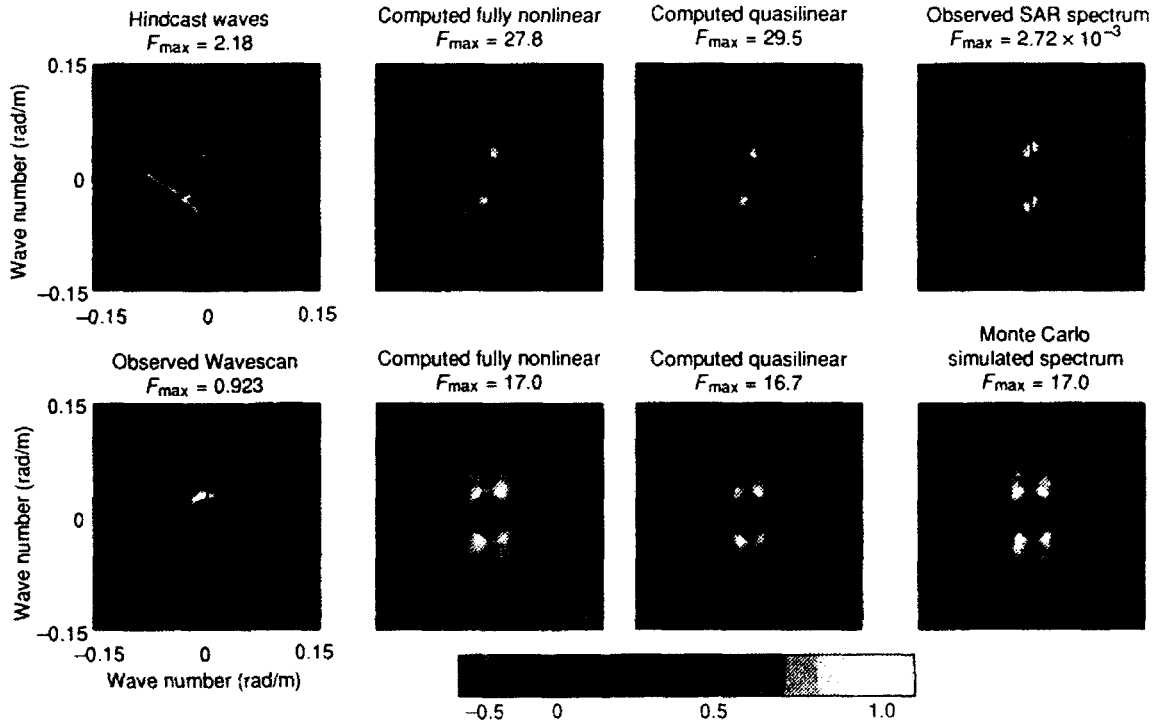

Figure 1. Hindcast (top row) and observed (Wavescan, bottom row) wave spectra together with computed SAR spectra for LEWEX run 1 over the *Tydeman*, 1219 UT on 14 March. The observed SAR spectrum is shown in the top right panel. The bottom right panel shows the Monte Carlo simulated SAR spectrum for the Wavescan wave spectrum. The aircraft flight direction is in the x-direction. Spectra are normalized with respect to the maximal spectral density F_{max} (given in units of m^4).

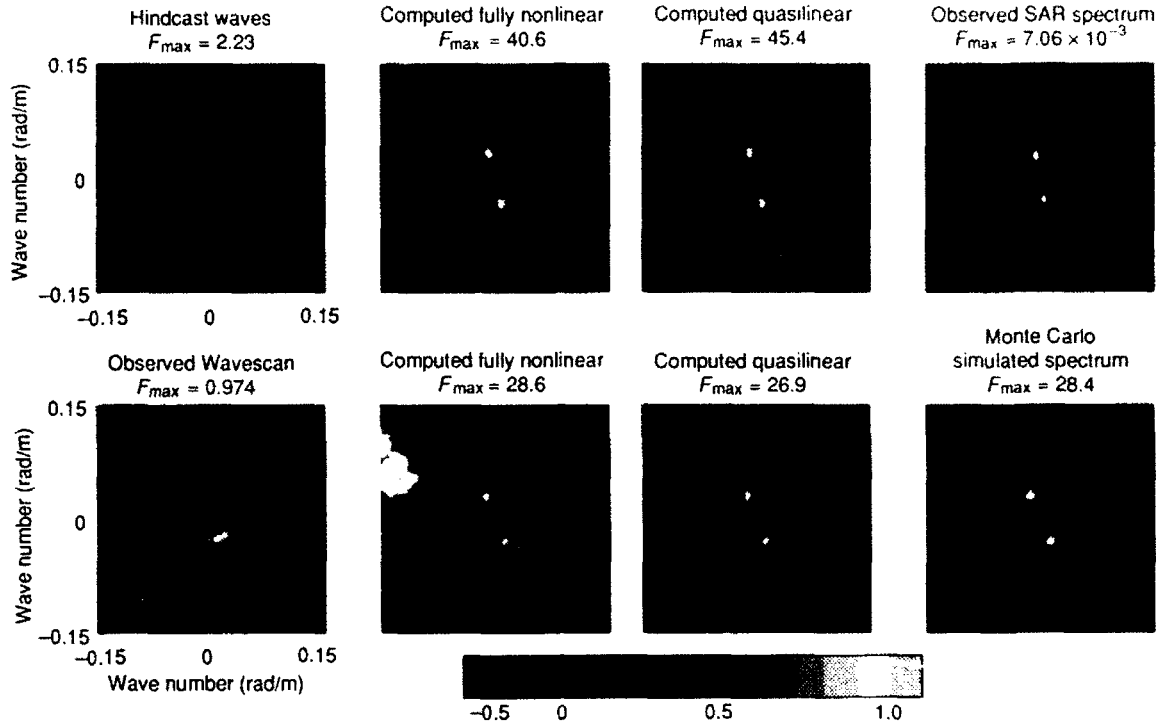

Figure 2. Same as Figure 1 but for LEWEX run 2 over the *Tydeman*, 1259 UT on 14 March. The aircraft flight direction is opposite that of run 1. Coordinates are defined as before in the aircraft frame.

figures correspond to different input wave spectra, shown in the left column. The Monte Carlo computations are shown only for the Wavescan spectra (second row).

Several features are apparent:

1. The SAR wave image spectra show little resemblance to the (symmetrized) input wave spectra. This is, of course, a well-known feature of SAR spectra. But perhaps it has not always been fully appreciated that the distortion can be pronounced not only for azimuthally traveling waves, for which the nonlinearities are large, but also for relatively linear range traveling waves, as in these examples.

2. The azimuthal cutoff is well defined and occurs at a lower wave number for the higher altitude flight, as expected.

3. The SAR spectra show evidence of some azimuthal asymmetry relative to the SAR look direction that is not apparent in the original wave spectra. The asymmetry depends on the wave propagation direction relative to the SAR look direction. In run 1 (Fig. 1), waves in the top right quadrant are enhanced relative to the waves in the top left quadrant, whereas in run 2 (Fig. 2), waves in the bottom right quadrant (corresponding to the top left quadrant in the 180° rotated spectrum of Fig. 1) are enhanced relative to the bottom left quadrant. The fact that the asymmetry depends on the SAR look direction—in both the simulations and the observations—is a clear indication that it represents an artifact of the imaging and is not a real feature of the wave spectrum.

4. The theoretical SAR spectra agree reasonably well with the measured SAR spectra in all cases. This, together with the features listed above, underlines the need for a first-guess input wave spectrum and the application of quantitative nonlinear mapping computations for the meaningful interpretation of measured SAR spectra.

5. The quasi-linear approximation (Eq. 32) yields a good first-order description, perhaps not surprising in these examples of relatively linear, predominately range-traveling waves.

6. The closed nonlinear transformation relation and the Monte Carlo computations yield essentially identical results. The small deviations between the Monte Carlo method and the closed integral computations near the azimuthal cutoff line can probably be attributed to the analytical Phillips form of the high-frequency tail of the spectrum used in the Monte Carlo computations as opposed to the modeled spectrum in the closed integral computations.

The distortions of the SAR spectra relative to the wave spectra can be explained rather simply by the structure of the SAR MTF, Equation 19. The azimuthal asymmetry is produced by interference between the frozen surface and velocity-bunching MTF's. The frozen-surface MTF is symmetrical about the look direction, whereas the velocity-bunching MTF is antisymmetrical (cf. Eqs. 5, 6, 16, and 17). Thus, while the square modulus of each MTF, taken by itself, is symmetrical about the look direction, the square modulus of the net complex SAR MTF, consisting of the sum of both MTF's is, in general, nonsymmet-

rical. It follows, moreover, that a change in sign of the look direction interchanges the enhanced and attenuated lobes of the wave spectrum, as seen in Figures 1 and 2.

The interference between the frozen surface and the velocity-bunching modulation can be identified explicitly in the expansion (Eq. 25). The relevant spectral distributions are shown in Figure 3 for run 1. The first term, $C \cdot P^S_{10}$ ($n = 1$, $m = 0$) (Fig. 3A), represents the frozen surface contribution (but with the inclusion of the azimuthal cutoff factor C). It is positive everywhere and reproduces the approximately symmetrical distribution of the wave spectrum about the SAR look direction. The second term, $C \cdot (k_x\beta)P^S_{11}$ ($n = 1$, $m = 1$) (Fig. 3B), represents the quadratic interference between the frozen surface and velocity-bunching transfer functions. It is asymmetrical, alternating in sign between quadrants. The third term, $C \cdot (k_x\beta)^2 P^S_{12}$ ($n = 1$, $m = 2$) (Fig. 3C), represents the pure (quasi-linear) velocity-bunching term, without the RAR contribution. It is positive and symmetrical. The sum of the first three terms yields the quasi-linear SAR spectrum, Equation 32 (Fig. 3D), which is shown also in the corresponding panel of Fig. 1. The asymmetry of the quasi-linear spectrum is seen to arise from the interference term. Asymmetries occur in general in all higher order, odd-m terms of the expansion (e.g., Figs. 3E and 3F), contributing to the asymmetry of the final nonlinear SAR spectrum (Fig. 3H). Figure 3G ($m = 10$) is an example of a higher order symmetrical spectral term. It exhibits a pronounced concentration along the azimuthal cutoff line that is characteristic of all higher order terms and arises from the product of the factor $(k_x\beta)^m$ with the exponential azimuthal cutoff factor C.

CONCLUSIONS

A new, closed, nonlinear, integral transform relation describing the mapping of a two-dimensional surface-wave spectrum into a SAR image spectrum has been presented and discussed for two LEWEX examples. The new transform relation offers a number of advantages. It is rapid and accurate enough to be applied routinely to the processing of quasi-continuous operational satellite SAR data. It offers a simple approach to the inverse problem of inferring the optimal wave spectrum from a measured SAR spectrum for a given first-guess wave spectrum (cf. Ref. 8). By expanding the integral transform in a Fourier transform series, it provides a clearer insight into the details of the mapping mechanisms. The expansion yields separate spectral contributions for the frozen-surface (RAR) modulation term, the linear velocity-bunching mechanism, the linear interaction between the two, and the higher order nonlinear velocity-bunching interactions and distortions. The azimuthal smearing caused by nonlinear velocity-bunching effects can be expressed very simply as an exponential cutoff factor that applies to all terms of the expansion.

The LEWEX examples demonstrate that SAR ocean-wave imaging theory is in good agreement with measurements. The SAR spectra can differ strongly from the input wave spectra so that a general quantitative interpretation of SAR image spectra in all cases is possible only

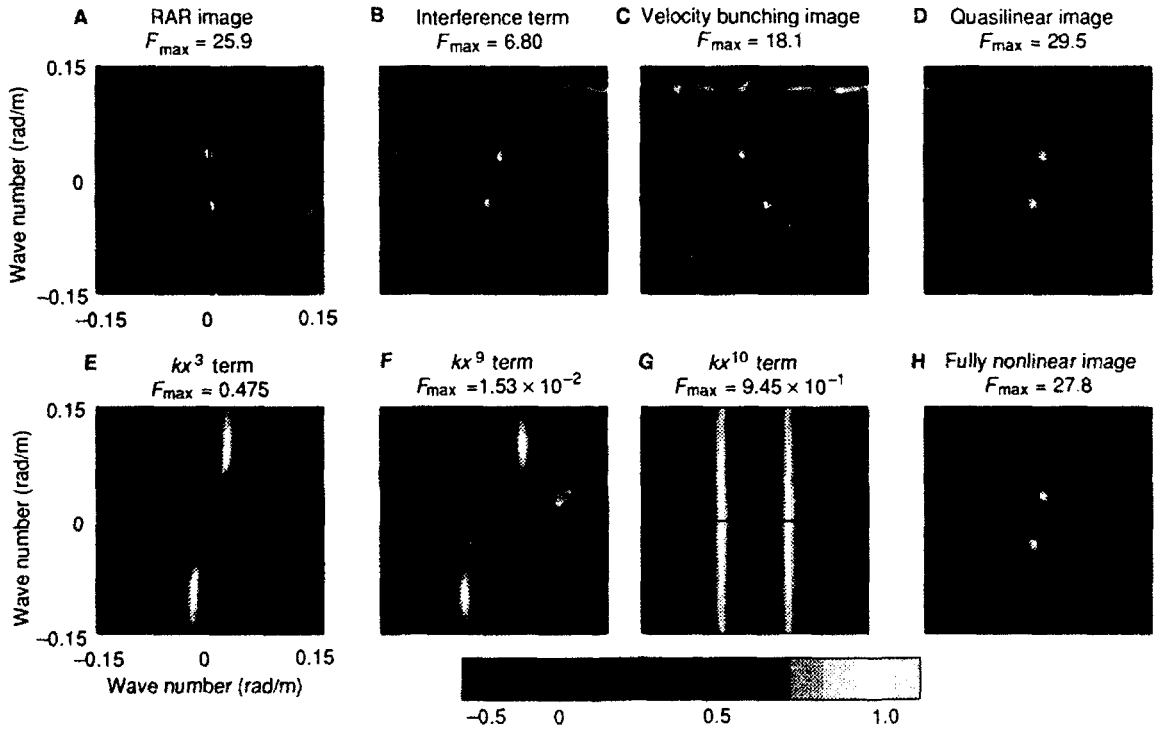

Figure 3. Contributions of various spectral expansion terms to the SAR spectral image for LEWEX run 1. Note the asymmetry about the look direction induced by the terms with odd m (k_x powers). The dominant asymmetry arises from the linear RAR velocity-bunching interference term ($m = 1$, $n = 1$).

with the aid of exact nonlinear transform computations and a reasonable first-guess wave spectrum derived from a model. The quasi-linear SAR image spectrum (the linear SAR spectrum augmented by the azimuthal cutoff factor) nevertheless provides a good quantitative approximation in many cases in which the nonlinearities are not too severe and also provides a useful qualitative description of the spectrum even for strongly nonlinear cases.

REFERENCES

[1] Hasselmann, K., Raney, R. K., Plant, W. J., Alpers, W., Shuchman, R. A., et al., "Theory of Synthetic Aperture Radar Ocean Imaging: A MARSEN View," *J. Geophys. Res.* **90**, 4659 (1985).

[2] Alpers, W., "Monte Carlo Simulations for Studying the Relationship Between Ocean Wave and Synthetic Aperture Radar Image Spectra," *Geophys. Res.* **88**, 1745 (1983).

[3] Alpers, W., Brüning, C., and Richter, K., "Comparison of Simulated and Measured Synthetic Aperture Radar Image Spectra with Buoy-Derived Ocean Wave Spectra during the Shuttle Imaging Radar-B Mission," *IEEE Trans. Geosci. Remote Sensing* **GE-24**, 559 (1956).

[4] Alpers, W., and Brüning, C., "On the Relative Importance of Motion-Related Contributions to the SAR Imaging Mechanism of Ocean Surface Waves," *IEEE Trans Geosci. Remote Sensing* **GE-24**, 873 (1986).

[5] Lyzenga, D. R., "Numerical Simulation of Synthetic Aperture Radar Image Spectra for Ocean Waves," *IEEE Trans. Geosci. Remote Sensing* **GE-24**, 863 (1986).

[6] Brüning, C., Alpers, W., Zambresky, L. F., and Tilley, D. G., "Validation of a SAR Ocean Wave Imaging Theory by the Shuttle Imaging Radar-B Experiment over the North Sea," *J. Geophys. Res.* **93**, 15,403 (1988).

[7] Brüning, K., Alpers, W., and Hasselmann, K., "Monte Carlo Simulation Studies of the Nonlinear Imaging of a Two-Dimensional Surface Wave Field by a Synthetic Aperture Radar," *Int. J. Remote Sensing* (1990).

[8] Hasselmann, K., and Hasselmann, S., "On the Nonlinear Mapping of an Ocean Wave Spectrum into a SAR Image Spectrum and Its Inversion" (submitted to *J. Geophys. Res.*).

[9] WAMDIG (Wave Model Development and Implementation Group), "The WAM Model—A Third-Generation Ocean Wave Prediction Model," *J. Phys. Oceanogr.* **18**, 1775-1810 (1988).

[10] Keller, W. C., and Wright, J. W., "Microwave Scattering and the Straining of Wind Generated Waves," *Radio Sci.* **10**, 139-147 (1975).

[11] Plant, W. J., Keller, W. C., and Cross, A., "Parametric Dependence of the Ocean Wave Radar Modulation Transfer Function," *J. Geophys. Res.* **88**, 9747-9756 (1983).

[12] Schroter, J., Feindt, F., Alpers, W., and Keller, W. C., "Measurement of the Ocean-Wave-Radar Modulation Transfer Function at 4.3 GHz," *J. Geophys. Res.* **91**, 932-946 (1986).

[13] Feindt, F., Schroter, J., and Alpers, W., "Measurement of the Ocean Wave-Radar Modulation Transfer Function at 35 GHz from a Sea Based Platform in the North Sea," *J. Geophys. Res.* **91**, 9701-9708 (1986).

[14] Alpers, W., and Hasselmann, K., "Spectral Signal-to-Clutter and Thermal Noise Properties of Ocean Wave Imaging Synthetic Aperture Radars," *Int. J. Remote Sensing* **3**, 423-446 (1982).

[15] Hasselmann, K., Hasselmann, S., Bauer, E., Brüning, C., Lehner, S., et al., *Development of a Satellite SAR Image Spectra and Altimeter Wave Height Data Assimilation System for ERS-1*, ESA contract report and MPI report No. 19 (1988).

[16] Beal, R. C., Tilley, D. G., and Monaldo, F. M., "Large- and Small-Scale Spatial Evolution of Digitally Processed Ocean Wave Spectra from SEASAT Synthetic Aperture Radar," *J. Geophys. Res.* **88**, 1761-1778 (1983).

[17] Monaldo, F. M., and Lyzenga, D. R., "On the Estimation of Slope- and Height-Variance Spectra from SAR Imagery," *IEEE Trans. Geosci. Remote Sensing* **GE-24**, 543-551 (1986).

[18] Monaldo, F. M., and Lyzenga, D. R., "Comparison of Shuttle Imaging Radar-B Ocean Wave Spectra with Linear Model Predictions Based on Aircraft Measurements," *J. Geophys. Res.* **93**, 15,374-15,388 (1988).

[19] Tucker, M. J., "The Imaging of Waves by Satellite Synthetic Aperture Radar: The Effects of Surface Motion," *Int. J. Remote Sensing* **6**, 1059-1074 (1985).